PCCP

Local structure and NO adsorption/desorption property of Pd^{2+} cations at different paired Al sites in CHA zeolite

Journal:	*Physical Chemistry Chemical Physics*
Manuscript ID	CP-ART-06-2021-002668.R1
Article Type:	Paper
Date Submitted by the Author:	22-Jul-2021

Complete List of Authors:	Yasumura, Shunsaku; Hokkaido University, Institute for Catalysis Ueda, Taihei; Hokkaido University, Institute for Catalysis Ide, Hajime; Hokkaido University, Institute for Catalysis Otsubo, Katsumasa; Hiroshima University, Graduate School of Advanced Science and Engineering Liu, Chong; Chinese Academy of Sciences Fujian Institute of Research on the Structure of Matter, Institute for Catalysis; Tsunoji, Nao; Hiroshima University, Graduate School of Advanced Science and Engineering Toyao, Takashi; Hokkaido university, Institute for Catalysis Maeno, Zen; Hokkaido University, Institute for Catalysis Shimizu, Ken-ichi; Hokkaido University, Catalysis Research Center

Local structure and NO adsorption/desorption property of Pd^{2+} cations at different paired Al sites in CHA zeolite

Shunsaku Yasumura[a], Taihei Ueda[a], Hajime Ide[a], Katsumasa Otsubo[b], Chong Liu[c], Nao Tsunoji[b], Takashi Toyao[a,d], Zen Maeno[a]*, Ken-ichi Shimizu[a,d]*

[a] Institute for Catalysis, Hokkaido University, N-21, W-10, Sapporo 001-0021, Japan

[b] Graduate School of Advanced Science and Engineering, Hiroshima University, Higashi-Hiroshima 739-8527, Japan

[c] State Key Laboratory of Structural Chemistry, Fujian Institute of Research on the Structure of Matter, Chinese Academy of Sciences, Fuzhou, Fujian 350002, China

[d] Elements Strategy Initiative for Catalysts and Batteries, Kyoto University, Katsura, Kyoto 615-8520, Japan

*Corresponding author

Zen Maeno

E-mail: maeno@cat.hokudai.ac.jp

Ken-ichi Shimizu

E-mail: kshimizu@cat.hokudai.ac.jp

ABSTRACT:

Recently, Pd-exchanged CHA zeolites (Pd-CHA) have attracted attention as promising passive NOx adsorbers (PNAs) for reducing NOx emissions during the cold start period of a vehicle engine. In this work, the relationship between the local structures and the NO adsorption/desorption properties of the Pd cations in CHA zeolites was investigated. Pd cation formation and NO adsorption were theoretically explored by density functional theory (DFT) calculations for different paired Al sites in six-/eight-membered rings (6MR/8MR). Furthermore, we prepared a series of Pd-CHAs with different Pd loadings (0.5–5.4 wt%) and evaluated their NO adsorption/desorption properties by *in-situ* infrared (IR) spectroscopy and temperature-programmed desorption (TPD) measurements. The increase in the Pd loading resulted in a shift in the NO desorption temperature toward a higher temperature regime. This phenomenon was ascribed to the increase in the proportion of less stable Pd cations, resulting in improved NO adsorption. Furthermore, the effect of Al distribution on the NO adsorption property of Pd-CHA was examined using CHA zeolites containing different proportion of paired Al sites in 6MR while maintaining similar Si/Al ratios (Si/Al = 12.0–16.5). The present study, based on a combination of theoretical and experimental techniques, shows that the NO adsorption/desorption properties over Pd-CHA can be tuned by controlling the Pd loading amount and the type of paired Al sites.

1. INTRODUCTION

The elucidation of the surface structure–function relationship of solid materials, such as heterogeneous catalysts and adsorbents, is a formidable task because solid surfaces are highly complex, and consequently, a variety of surface active sites are present.[1–10] Zeolites are widely employed in industrial processes, including adsorption[11–15] and catalysis.[16–25] Compared to bulk metal oxides, zeolites are regarded as well-defined solid supports owing to the regularity of their frameworks and the cation exchange ability of Al sites. By exploiting these characteristics, atomic metal cations can be immobilized on zeolites. However, even for zeolite-based materials, the positions and densities of Al sites are nonuniform, which possibly affects the local structure and functionality of the exchanged metal cations.[26–30] The atomic-scale understanding of the non-uniformity of cation-exchanged zeolites and its effect on functionalities has recently attracted significant attention, owing to the advances in experimental and theoretical techniques, which have provided essential insights for developing more effective zeolite-based materials.[31–36]

Pd-exchanged zeolites are considered as efficient catalysts for CH_4 oxidation and the selective catalytic reduction of NO by CH_4 (CH_4-SCR).[37–39] Recently, they were applied as passive NOx adsorbers (PNAs) that capture NOx in low-temperature regions (typically < 100 ˚C) at the upstream of the NH_3-SCR system, to reduce the NOx emission during the cold start period of a vehicle engine and, subsequently, release the stored NOx in high-temperature regions (typically 250–400 ˚C) after the catalyst has reached the operating temperature .[11,12,40] The development of efficient PNAs is highly desired because rich regeneration process, which is required for Lean NOx traps, can be avoided via thermal regeneration.[41,42] Atomically dispersed Pd^{2+} cations are responsible for NO adsorption and desorption.[43,44] Among the various Pd-exchanged zeolites, Pd-CHA has attracted attention because of its high NOx desorption temperature and the superior hydrothermal stability of the CHA framework compared to those of other zeolites.[44–50] Szanyi and co-workers conducted experimental and theoretical characterizations of the Pd cation in CHA zeolite and revealed that the zeolite framework can stabilize electrophilic Pd^{2+} cations.[44] The same group also achieved improvements in the NOx storage capacity and time for NOx removal by increasing the loading of Pd cations.[51] For the NOx desorption properties, two desorption peaks appeared in low- and high-temperature regions (around

250 and 400 ˚C, respectively), as demonstrated in the NOx temperature-programmed desorption (NOx-TPD) measurements.[48,52] Although these peaks were indicative of the desorption from two kinds of Pd cation sites, their detailed structures and the origin of the difference in the desorption temperatures were unclear. Quite recently, Epling and Paolucci revealed that a bare Pd^{2+} cation at the paired Al site in the six-membered ring (6MR) of the CHA framework is the most stable and that its NO adsorption property is sensitive to reaction conditions based on a combined approach of experiments and computational modeling.[49] Additionally, Khivantsev *et al.* reported that the hydrothermal stability of loaded Pd cations was improved by the relatively high amount of paired Al sites in the CHA zeolite.[53] Gounder's group carried out a detailed speciation of the Pd cationic species in CHA zeolite and revealed Pd agglomeration and their subsequent redispersion to mononuclear Pd^{2+} ions, which prefer binding at 6MR paired Al sites in the CHA zeolite.[54] Despite the aforementioned experimental and theoretical studies on Pd-CHA, the local structures of the Pd cations at different paired Al sites and their relationship with the NO adsorption/desorption properties have not been addressed yet. One of the experimental obstacles for the elucidation of this relationship is the difficulty of loading Pd cations in concentrations of more than 1 wt% into CHA zeolites via the conventional aqueous phase ion-exchange method, which is attributed to the strong water solvation of cations that are too bulky to disperse into the small pores.[55]

Recently, our group developed a simple preparation method of Pd-CHA with high loadings via a NO-facilitated oxidative solid-state ion-exchange reaction, where ca. 80–90% of bulk Pd (up to 5.4 wt%) are transformed into atomically dispersed Pd cations (maximum loading of Pd cations: 4.1 wt%).[56] The developed method enabled the preparation of Pd-CHA zeolites with a wide loading range of Pd cations. Here, we investigated the relationship between the local structures of Pd^{2+} cations and their NO adsorption/desorption properties using a combination of theoretical and experimental approaches. First, the stabilities of the Pd^{2+} cations at different paired Al sites in 6MR/8MR and their NO adsorption energies were assessed by density functional theory (DFT) calculations. It was found that the stability of the Pd^{2+} cations strongly depends on the type of paired Al sites and that less stable Pd^{2+} cations result in increased NO adsorption strength. The NO desorption temperatures and molecular orbitals of the Pd^{2+} cations were also theoretically studied. Additionally, we experimentally investigated the

NO adsorption/desorption properties of Pd-CHA with different loadings by *in-situ* infrared (IR) and NO-TPD measurements. The increase in the Pd loading increased not only the NO adsorption capacity but also the NO desorption temperature and the adsorption energy. The dependency of the desorption temperature on the Pd loadings can be ascribed to the increase in the proportion of less stable Pd^{2+} cations. Moreover, CHA zeolites with different Al distributions and similar Si/Al ratios were prepared and subsequently applied to investigate the effect of the type of Al sites on the NO adsorption properties.

2. THEORETICAL and EXPERIMENTAL SECTION

2.1. DFT calculation

Spin-polarized DFT calculations were conducted under periodic boundary conditions using the Vienna ab-initio simulation package (VASP).[57–59] A plane wave cut-off energy of 500 eV was applied. The generalized gradient approximated Perdew–Burke–Ernzerhof (GGA-PBE) functional was employed.[60,61] Brillouin zone sampling was set to only the Γ point.[62] The CHA unit cell used in this study is shown in Fig. 1 During the calculations, the lattice constants of the CHA zeolite were fixed at values given in the International Zeolite Association (IZA) database (a = b = 13.675 Å, c = 14.767 Å, α = β = 90.0°, and γ = 120°).[63] To discuss the molecular-orbital interactions, cluster calculations were employed with the Gaussian 16 package. The hybrid ωB97X-D functional, which was well applied for the evaluation of the relative energy of zeolite[64–66], was used with the 6-31G** basis sets and SDD basis sets for Si, Al, O, and H atoms and Pd atoms, respectively[67,68]. Charge decomposition analysis (CDA) was performed using the Multiwfn program.[69]

2.2. Experimental details

A series of Pd-CHAs with different loadings (0.5–5.4 wt%) were prepared *in-situ* via NO-facilitated atomic dispersion according to the procedure in our recent paper[56] and subsequently used for NO adsorption/desorption experiments. For the NO adsorption monitored by Fourier transform infrared spectroscopy (FTIR), a self-supported disk (diameter: 20 mm, weight: approx. 50 mg) of Pd-CHA was prepared in a home-made *in-situ* IR cell and subsequently exposed to a flow of 0.1% NO/He (the schematic view of the used *in-situ* IR setup was shown in Fig. S1). The adsorbed NO species were monitored by IR spectroscopy (JASCO FT/IR-4600 spectrometer). Twenty scans were accumulated for each spectrum, and a triglycine sulfate (TGS) detector was applied. Before adsorption, the background spectra were measured at each temperature (100–400 °C) under the He flow. Three types of CHA zeolites with different portions of paired Al sites were prepared according to a previous paper.[70] NO-TPD measurements were performed using a fixed-bed continuous flow system to investigate the effect of Al distributions on the NO adsorption properties of Pd-CHA. The *in-situ* prepared Pd-CHA (80 mg) was cooled to 350 °C under a He flow after NO treatment. The NO concentration in the outlet gas was monitored by a home-made gas cell equipped with CaF_2 windows

using the same IR spectroscopy. During the first 400 s, a flow of 0.1% NO/He passed through a bypass line. After data recording for 400 s, the flow was switched to the reactor. At 1000 s, the temperature of the reactor was increased at a rate of 20 ˚C/min and subsequently maintained at 750 °C. More details on the methodology are provided in the ESI.

3. RESULTS AND DISCUSSIONS

3.1. Formation of Pd^{2+} cations at different paired Al sites in CHA zeolite

A CHA zeolite is composed of a rhombohedral unit cell with two cage sizes, forming four-, six-, and eight-membered rings (4MR, 6MR, and 8MR, respectively). Several kinds of two Al sites were considered as the exchange sites for bare divalent cations regardless of different description, such as paired and close unpaired Al sites.[32,49,71–76] For the theoretical investigation in the present study, five paired Al sites: 6MR(3NN), 8MR(2NN), 8MR(3NN), 8MR(4NN), and 5NN, were considered as the model sites for the stabilization of Pd^{2+} cations. These models are also considered as possible two Al sites in the recent theoretical studies.[49,76,77] Although the valence states of Pd cations on the considered models (especially on 5NN) are still controversial[49,76,77], these models were applied to explore the effect of Al–Al distance on the NO adsorption. The model sites can be distinguished by the type of sharing ring and the number of Si centers connecting two Al sites (Fig. 1) For example, the paired Al site with a connectivity distance of 3 (Al−O−(Si−O)$_2$−Al) in 6MR is labeled as 6MR third-nearest-neighbor, i.e., 6MR(3NN). For 5NN, each Al site exists in 6MR and 8MR and is connected by a distance of 5 (Al−O−(Si−O)$_4$−Al). The Al−Al distances are different in the range of 5.74–9.71 Å among the five paired Al sites.

The stability of the Pd cations at different paired Al sites was theoretically evaluated. Fig. 2 shows the optimized structures, and Table 1 summarizes the distance between the Pd^{2+} cation and each Al site (Al1 and Al2 denote the close Al site and the far Al site, respectively). For 6MR(3NN), a Pd^{2+} cation is located at almost the center of 6MR to minimize both the distances of Pd−Al1 and Pd−Al2 for charge compensation.[49,78] For 8MR(2NN), (3NN), (4NN), and 5NN sites, the Pd^{2+} cations are located at the center of 6MR to maintain suitable distances with Al1 (ca. 2.86 Å), while the distance from Al2 is greater (5.43–8.51 Å). Other examined configurations of Pd^{2+} cations on each paired Al site are provided in ESI (Fig. S2). The relative formation energies of the Pd cations (ΔE_f) are listed in Table 1. We also calculated ΔE_f for the Pd^{2+} cations at 8MR in 8MR(2NN), 8MR(3NN), 8MR(4NN), and 5NN sites and then compared with the above results (Fig. S2 in ESI). The ΔE_f value of the Pd^{2+} cation at 6MR is lower than one at 8MR in all case. The ΔE_f value for 6MR(3NN) is the lowest among all the models (2.06 eV), which is consistent with the calculation results reported by Epling and Paolucci.[49]

The ΔE_f value increased in the order of 6MR(3NN) < 8MR(2NN) < 8MR(3NN) < 8MR(4NN) < 5NN. As the Pd–Al2 distance increases (2.92–8.51 Å), ΔE_f increases, which indicates that a long Pd–Al2 distance is unfavorable for the stabilization of the Pd^{2+} cation due to the difficulty of charge compensation with Al sites.[49,78]

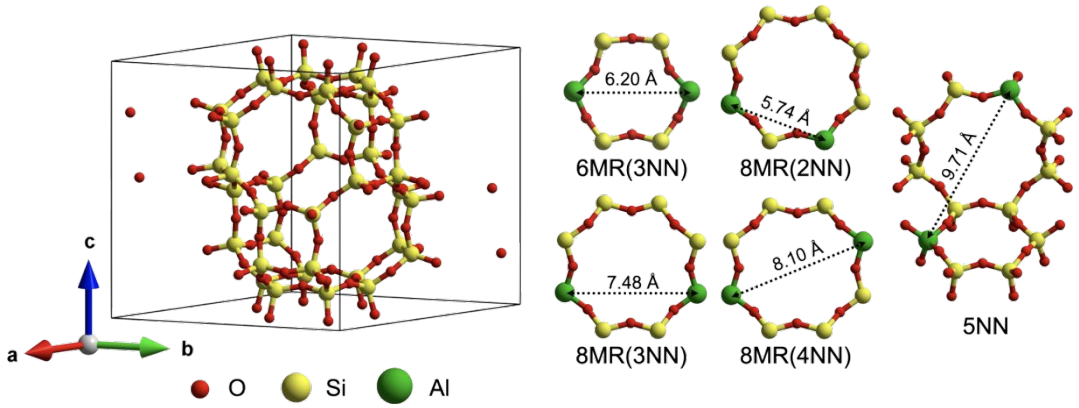

Fig. 1 A unit cell of CHA zeolite and the considered paired Al sites in periodic DFT calculations.

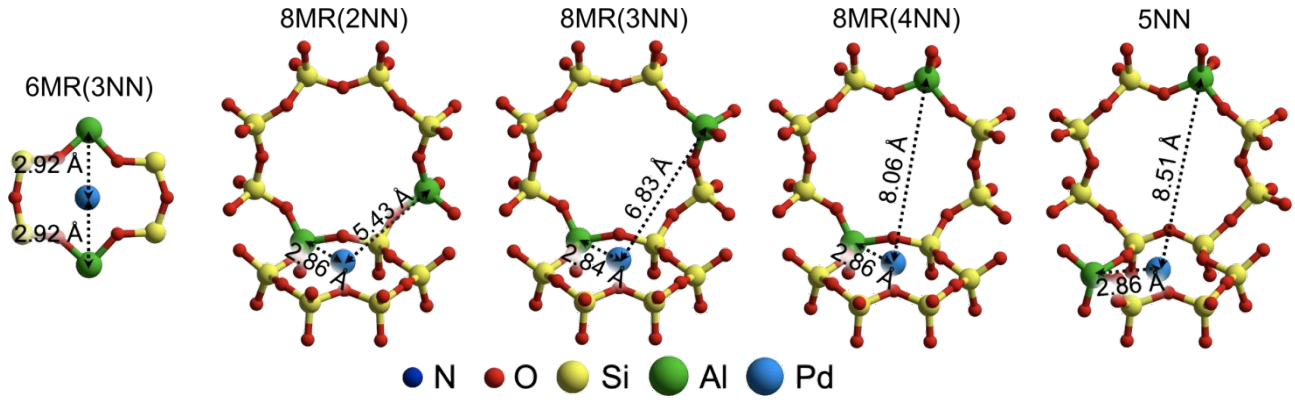

Fig. 2 Optimized structures of Pd cations at different paired Al sites in CHA zeolites. Al1 and Al2 denote the close and far Al sites, respectively. Only the atoms around the Pd cation are shown for clarity. The structural information (CONTCAR files) of all the considered structures are provided in ESI.

Table 1 Pd–Al distances and relative formation energy of the Pd cations at different paired Al sites.

Paired Al sites	Pd–Al1 (Å)	Pd–Al2 (Å)	Relative formation energy (ΔE_f)[a] (eV)
6MR(3NN)	2.92	2.92	2.06
8MR(2NN)	2.86	5.43	3.18
8MR(3NN)	2.84	6.83	3.63
8MR(4NN)	2.86	8.06	3.67
5NN	2.86	8.51	3.75

[a] ΔE_f is defined in ESI.

3.2 NO adsorption on each Pd^{2+} cation at different paired Al sites

The NO adsorption on Pd^{2+} cations was also theoretically investigated for different paired Al sites. Fig. 3 shows the optimized structure of the NO-adsorbed Pd cations. Their adsorption energies (E_{ad}) and geometric parameters (Pd–N bond length and Pd–N–O angle) are listed in Table 2. E_{ad} negatively increases from −1.04 to −1.74 eV in the following order: 6MR(3NN) < 8MR(2NN) < 8MR(3NN) < 8MR(4NN) < 5NN. This order is the same as the order of increase in ΔE_f. As the NO adsorption energy increases negatively, the Pd–N bond length decrease in the range of 1.77–1.92 Å. The adsorption geometry was bent in all the considered structures (Pd–N–O angles: 121.1–158.1°). Similar adsorption structures were reported in a previous study on Pd-MOR, where the NO molecule preferentially adsorbed at a Pd–N–O angle of ca. 130°, due to the electronic interaction of the dσ and dπ orbitals of the Pd^{2+} cation with a singly occupied antibonding π* molecular orbital (SOMO) of the NO molecule.[78]

Raybaud *et al.* theoretically investigated the NO adsorption on the Pd^{2+} cations in Pd-MOR, where the adsorption strength of NO depends on the empty Pd electronic levels just about the Fermi energy level, inducing the transfer of electrons from the SOMO of NO to the d states of Pd.[78] Inspired by their study, the correlation between the lowest unoccupied molecular orbital (LUMO) energy level of the Pd cation and the corresponding NO adsorption energy was further investigated in this study. The levels of the LUMO of the Pd cation and the SOMO of the NO molecule were calculated using the Gaussian 16 software. The cluster models used for this analysis were prepared by cutting out from the optimized periodic models (Fig. S3 in ESI). As shown in Fig. 4a, the energy level of the LUMO of the Pd cation becomes low as the stability of the Pd^{2+} cation decreases. The NO adsorption energies for all considered models are plotted as a function of the energy difference between the LUMO of the Pd cation and the SOMO of the NO molecule (ΔE_{dif}) to assess their interaction (Fig. 4b). A linear correlation was observed between E_{ad} and ΔE_{dif} (R^2 = 0.9861), indicating that the strong NO adsorption with few stable Pd cations is derived from the strong interaction between the LUMO of the Pd cation and the SOMO of the NO molecule.[79] This consideration was supported by the orbital interaction diagram depicted by CDA[80] in which the main component of the SOMO of the NO-adsorbed Pd cation in CHA zeolite is the LUMO of Pd (76%), indicating the transfer of electrons from

the SOMO of NO into the empty orbital of the Pd cation (Fig. 4c).

The vibration analysis of the adsorbed NO species revealed that the vibration frequencies were red-shifted (1861.0–1869.5 cm^{-1}) in comparison with the gas-phase value (1904 cm^{-1}) in all considered structures, except for the unstable Pd cation at 5NN (1906.1 cm^{-1}). The calculated frequencies are comparable with reported theoretical values[49,78,81], as well as experimental values.[38,49,82] Note that the stretching frequency of the NO molecule on unstable Pd cations was calculated to be too high, possibly due to the exchange splitting of Pd d-states.[78] Furthermore, to assess the effects of the experimental conditions, including temperature and partial pressures of gaseous molecules,[49] a thermodynamic analysis was performed to obtain the phase diagrams predicting the NO desorption temperature for the considered Pd cationic sites (Fig. S4). It was demonstrated that the NO desorption temperatures varied depending on the sites, and the difference in the temperature was estimated to be approximately 300 °C between 6MR(3NN) and 5NN. In summary, the type of paired Al site strongly affects the stability of Pd cations, as well as the NO adsorption toward high desorption temperatures, where strong NO adsorption occurs on few stable Pd cations. This is attributed to the strong interaction between the LUMO of the Pd cation and the SOMO of the NO molecule.

Table 2 The geometric parameters, adsorption energies for the NO structure, and calculated stretching frequency.

Configuration of paired Al sites	Pd–N (Å)	Pd–N–O (˚)	Adsorption energy (E_{ad}) (eV)	Vibrational frequency[a] (cm^{-1})
6MR(3NN)	1.92	121.1	−1.04	1861.5
8MR(2NN)	1.90	124.6	−1.36	1869.5
8MR(3NN)	1.87	127.1	−1.54	1861.0
8MR(4NN)	1.79	143.8	−1.68	1864.1
5NN	1.77	158.1	−1.74	1906.1
Gas-phase	–	–	–	1904

[a] The calculated frequencies were scaled by a factor of 0.9908. This value was defined from the experimental value (1904.1 cm^{-1})[83,84] and the calculated frequency of the gas-phase NO molecule (1921.8 cm^{-1}).

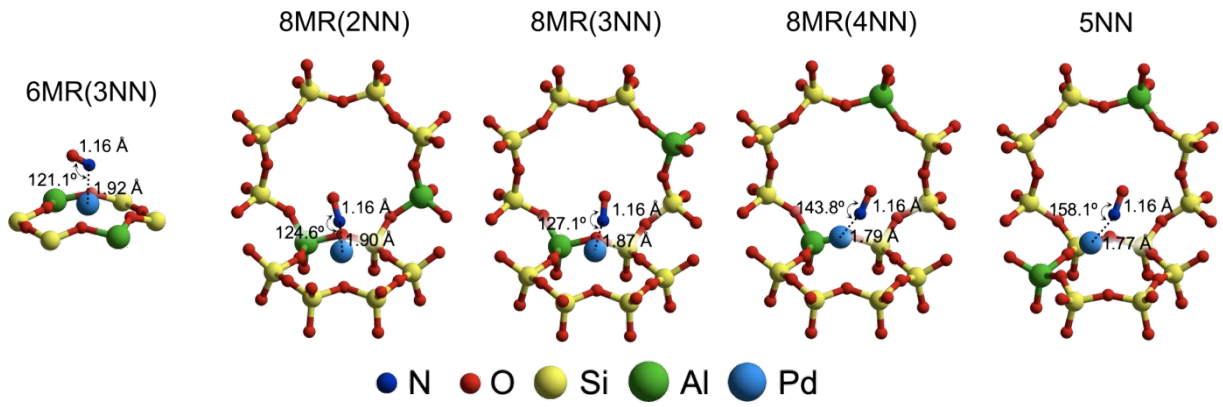

Fig. 3 Optimized structures of NO adsorption on the Pd^{2+} cations located at 6MR(3NN), 8MR(2NN), 8MR(3NN), 8MR(4NN), and 5NN sites in CHA zeolite (Only the atoms around the Pd cation are shown for clarity).

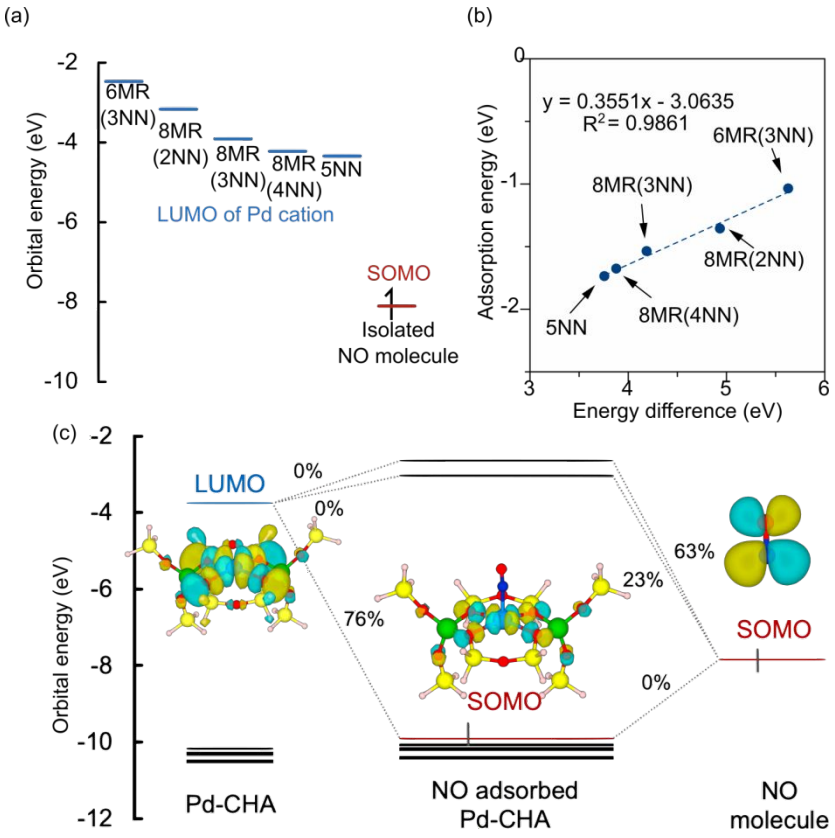

Fig. 4 (a) Energy levels of the LUMO of Pd at different paired Al sites and the SOMO of an isolated NO molecule. Blue lines and a red line represent the LUMO of Pd and the SOMO of NO, respectively. (b) The correlation of the NO adsorption energy and the energy difference between the LUMO of Pd and the SOMO of NO. (c) Orbital interaction diagram of α-spin, determined by CDA for the cluster model of the NO-adsorbed Pd cations at 6MR(3NN). (Yellow: Si, Red: O, Green: Al, Blue: N, Cyan: Pd, White: H).

3.3. *In-situ* IR measurement for NO adsorption on Pd-CHA with different Pd loadings

To experimentally investigate the relationship between the stability of Pd cations and the NO adsorption properties, a series of Pd-CHAs with different Pd loadings (0.5–5.4 wt%) were prepared through our preparation method, which utilizes a NO-facilitated solid-state ion-exchange reaction.[56] The prepared Pd-CHAs were used for static NO adsorption experiments monitored by *in-situ* IR spectroscopy. The IR spectra were collected after the intensity of the band derived from NO on the Pd^{2+} cation ($NO\text{-}Pd^{2+}$) around 1860 cm^{-1} reached equilibrium under a flow of 0.1% NO. The IR spectra obtained at different temperatures for 0.5 and 5.4 wt% Pd-CHA are shown in Fig. 5a and 5b, respectively (the IR spectra for the samples with other loadings are shown in ESI (Fig. S5)). The IR peak area of $NO\text{-}Pd^{2+}$ over 5.4 wt% Pd-CHA was significantly higher than that over 0.5 wt% Pd-CHA. Based on the absorption coefficient,[56] the amounts of adsorbed NO species over 0.5 and 5.4 wt% Pd-CHAs are determined as 0.04 and 0.41 mmol/g, respectively, corresponding to NO/Pd = 0.86 and 0.77 (NO/Pd denotes the molar ratio of the adsorbed NO to the total Pd amount). This indicates that c.a. 80% of the introduced Pd species are present in cationic state. In this way, large Pd particles were not observed by XRD and STEM measurements.[56] The IR band was clearly observed even at 400 °C over 5.4 wt% Pd-CHA, while the band was scarcely observed in the same temperature region over 0.5 wt% Pd-CHA. The peak top positions were varied depending on the Pd loading amount and temperature in the range of c.a. 1850–1870 cm^{-1}, agreed with our theoretical results. Fig. 5c shows the normalized areas of the IR band around 1860 cm^{-1} over Pd-CHA with different Pd loadings (0.5–5.4 wt%) as a function of temperature. The IR band areas were normalized by those obtained at 100 °C. Note that the shoulder peak around 1810 cm^{-1}, which is assignable to NO on the Pd^{+} cation, is included in the calculation of the area.[44,55] In all cases, the normalized areas decreased with the increase in the adsorption temperature. The areas for the 0.5 and 1 wt% Pd-CHAs drastically decreased in the region from 100 °C to 300 °C and nearly reached zero in the high-temperature region. In contrast, the IR bands were still noticeably observed at 400 °C for 2–5.4 wt% Pd-CHAs. To compare the stability of NO adsorption in the high-temperature region, the normalized areas at 400 °C were plotted as a function of the corresponding Pd/Al ratio in Fig. 5d. The normalized area increased with the loading. This dependency implies that the increase in the Pd loading induces the formation of less

stable Pd cations, which increases the NO adsorption strength.

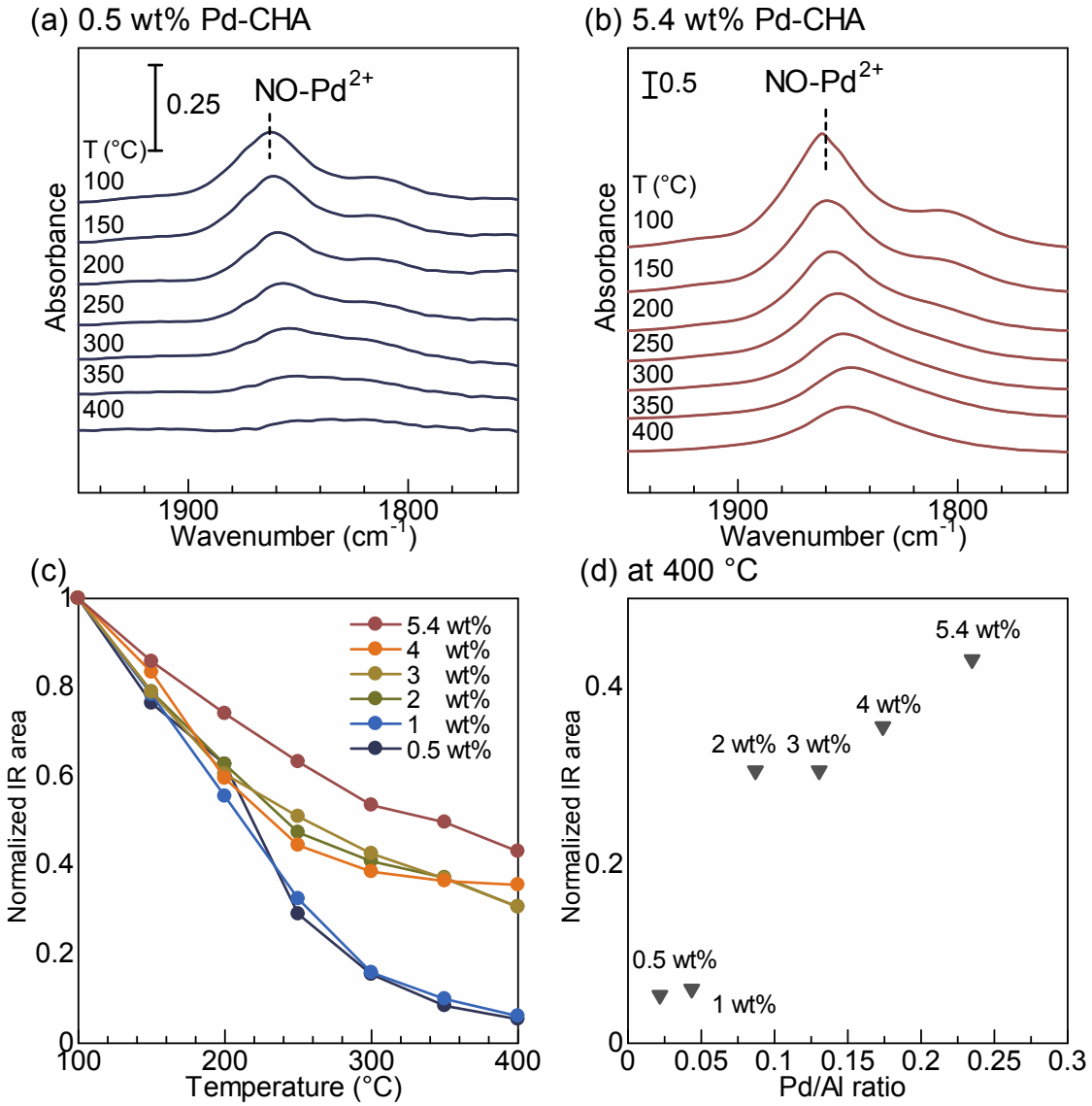

Fig. 5 *In-situ* IR spectra of NO–Pd^{2+} species over (a) 0.5 wt% and (b) 5.4 wt% Pd-CHAs under a flow of 0.1% NO (total flow: 100 mL/min). The background spectra were recorded under He flow at each measuring temperature before introducing the NO flow. (c) Temperature dependency of the normalized IR band area around 1860 cm^{-1} for different Pd loadings (0.5–5.4 wt%). (d) The normalized IR band area around 1860 cm^{-1} at 400 ˚C as a function of the Pd/Al ratio.

3.4. The dependency of the NO adsorption on the proportion of paired Al sites in 6MR

Gounder's group reported that the proportion of paired Al sites in 6MR of CHA zeolite can be tuned by controlling the ratio of inorganic and organic templates during the hydrothermal synthesis.[70] To investigate the effects of the differences in the proportion of paired Al sites, three kinds of CHA zeolites having different proportions of paired Al sites in 6MR (0.7%, 2.2%, and 7.1% in the total Al site) with a similar Si/Al ratio (Si/Al = 12.0−16.5) were synthesized according to the previous papers mentioned above. Thereafter, they were applied to prepare 1 wt% Pd-CHA($Al_{6MR\ pair}$/Al) ($Al_{6MR\ pair}$/Al denotes the relative portion of paired Al sites in 6MR) for NO adsorption. The $Al_{6MR\ pair}$/Al values were determined by an aqueous-phase ion-exchange reaction of the corresponding H^+-CHA with Co^{2+} cations (details are provided in ESI). Note that the actual ions-exchange sties for Co^{2+} cations are still controversial because the experimental conditions possibly affect the amount of exchanged Co^{2+} cations and their sites. Sklenak et al. investigated Co^{2+} ion-exchange into Na^+- and NH_4^+-CHA where both paired and close unpaired Al sites accommodate bare and hydrated Co^{2+} ions.[74,75]. The peak areas at 100 °C were similar among three 1 wt% Pd-CHA(0.7), (2.2), and (7.1) (Fig. S6), indicating that the Si/Al ratio does not significantly affect the NO adsorption at low temperature. Despite using the same Pd loadings, the normalized areas in the high-temperature region above 300 °C increased with the decrease in $Al_{6MR\ pair}$/Al (Fig. 6a). A linear correlation between the normalized IR area at 300 °C and $Al_{6MR\ pair}$/Al was observed (Fig. 6b). This result indicates that the paired Al sites in 6MR, such as 6MR(3NN), are responsible for the weak NO adsorption, owing to the formation of stable Pd cations; it also supports the occurrence of strong NO adsorption on Pd cations in paired Al sites in 8MR (8MR(2NN), (3NN), and (4NN)) or those between 6MR and 8MR (5NN).

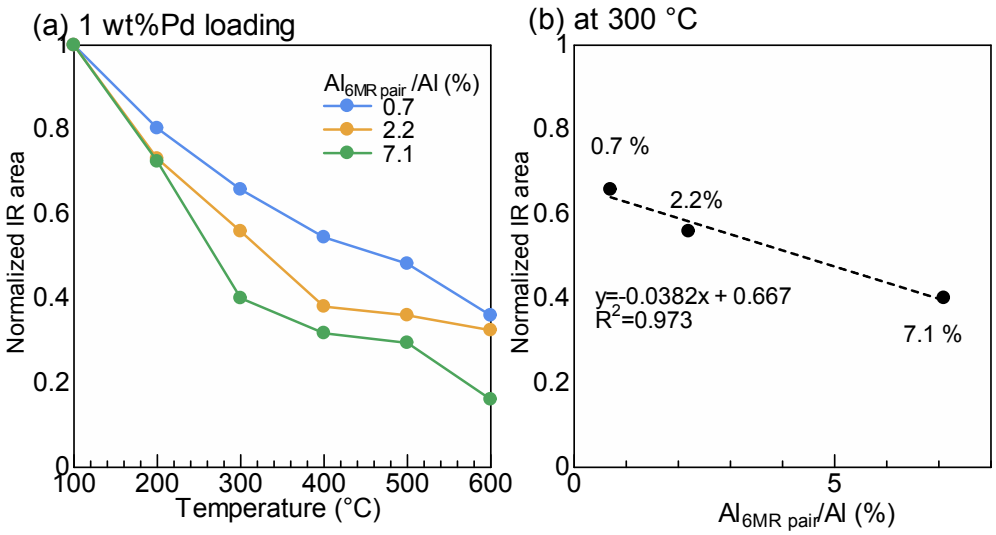

Fig. 6 (a) Temperature dependence of the normalized IR band area around 1860 cm^{-1} over 1 wt% Pd-CHA with different $Al_{6MR\ pair}/Al$ values (0.7, 2.2, 7.1 %), under a flow of 0.1% NO (total flow: 100 mL/min). (b) The normalized IR band areas around 1860 cm^{-1} at 300 ˚C as a function of $Al_{6MR\ pair}/Al$.

3.5. NO-TPD measurement of Pd-CHA with different Pd loadings

Finally, the NO desorption properties of Pd-CHA with high loadings (2–5.4 wt%) were examined by TPD measurements using a fixed-bed continuous flow system.[45,51,85] After the solid-state ion-exchange reaction was performed *in-situ* as explained above, the temperature of the reactor was set to 350 °C for NO adsorption. Note that the formation of NO^+ species at zeolite anions is unlikely to occur at 350 ˚C.[86] The obtained TPD profiles are shown in Fig. 7. Once the feed was switched to the reactor, a negative peak was observed for all the Pd-CHAs, corresponding to the NO adsorption. The area of the negative peak increased with the Pd loading, confirming that more NO species were captured. During the temperature increase, two positive peaks were observed, attributed to NO desorption. For the 2 wt% Pd-CHA, the main desorption peak was observed around 350−450 °C, while the second peak area, observed at a higher temperature of approximately 450 °C, was relatively small. With an increase in the Pd loading, the second desorption peak shift toward high temperatures, indicating that increasing the Pd loading increases the NO adsorption strength. The amounts of NO adsorption/desorption determined by the peak areas increases with the increase in Pd loading amount (Table S2). These results are consistent with those obtained by static NO adsorption experiments using *in-situ* IR spectroscopy.

To specify the Pd cations responsible for the NO desorption in the low- and high-temperature regimes, the adsorption energies corresponding to the observed NO desorption peaks were experimentally evaluated using the Redhead equation[87] (see ESI) and subsequently compared with the theoretically estimated values by DFT calculation (Table 3). The adsorption energies for the low-temperature desorption (E_{low}) were determined to be approximately 1.40 eV, whereas those for the high-temperature desorption (E_{high}) ranged from −1.57 to −1.83 eV. Compared with the theoretical values (Table 3), the low- and high-temperature NO desorption can be ascribed to the Pd cations on 8MR(2NN) (E_{ad} = −1.36 eV) and those on other paired Al sites, i.e., 8MR(3NN), 8MR(4NN), and 5NN (E_{ad} = −1.54 to 1.74 eV)), respectively, demonstrating that strong NO adsorption likely occurs on unstable Pd cations.

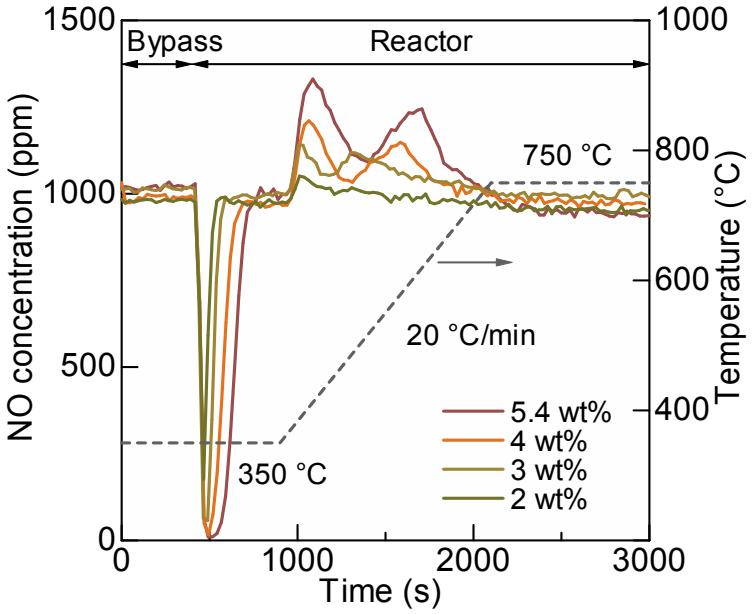

Fig. 7 NO adsorption at 350 °C for 600 s, followed by TPD (20 °C/min up to 750 °C) under a flow of 0.1% NO (He balance, total flow: 100 mL/min). The flow passed through a bypass line in the first 400 s.

Table 3 Comparison of the experimental and theoretical NO adsorption energies.

		NO adsorption energy (eV)	
		E_{low}[a]	E_{high}[b]
Exptl.	2 wt% Pd-CHA	−1.36	−1.57
	3 wt% Pd-CHA	−1.36	−1.57
	4 wt% Pd-CHA	−1.38	−1.76
	5.4 wt% Pd-CHA	−1.40	−1.83
		E_{ad}[c]	
Theor.	8MR(2NN)	−1.36	
	8MR(3NN)	−1.54	
	8MR(4NN)	−1.68	
	5NN	−1.74	

[a] Experimental adsorption energy of NO desorption at low temperatures. [b] Experimental adsorption energy of NO desorption at high temperatures. [c] Theoretical adsorption energy of Pd cations at different paired Al sites.

4. CONCLUSION

Herein, we revealed the relationship between the atomic-scale structure of the Pd^{2+} cations in CHA zeolite and the NO adsorption/desorption property by a combined approach of DFT calculations, *in-situ* IR spectroscopy, and NO-TPD measurement. First, the stability of the Pd^{2+} cations and the strength of the NO adsorption over Pd species located at five different 2Al sites were assessed using DFT calculations, which revealed that less stable Pd^{2+} cations afforded strong NO adsorption. As expected from the theoretical investigation, *in-situ* IR and NO-TPD measurements revealed that the NO desorption temperature increased with the Pd loading amount (up to 5.4 wt%). It was also observed that the amount of NO adsorbed in the high-temperature region increased upon decreasing the proportion of paired Al sites in 6MR in the CHA zeolite support, despite using the same Pd loading, indicating that weak NO adsorption is likely to occur on Pd cations at 6MR(3NN). For strong NO adsorption, the experimental adsorption energies of the NO desorption at low (350–450 °C) and high (> 450 °C) temperatures agree reasonably with the theoretically estimated values of the moderately stable Pd cations at 8MR(2NN) and the relatively unstable ones at 8MR(3NN), 8MR(4NN), and 5NN. This study not only revealed the dependency of the local structure and NO adsorption/desorption properties of Pd cations on the structure of the Al sites in CHA zeolites, but also demonstrated the tunability of Pd-CHA functions as PNAs by controlling the Pd loading amount and the distribution of Al sites.

Author contributions

S.Y. performed DFT calculation by using Gaussian software and wrote the draft. T.U. conducted in-situ IR experiment and NO-TPD measurement as well as DFT calculation by using VASP software. H.I. prepared Pd-loaded CHA zeolite. K.O. and N.T. synthesized CHA zeolites containing the different proportion of paired Al sites. C.L., T.T., and Z.M. critically revised the manuscript. K.S. designed and supervised the whole project.

Conflicts of interest

There are no conflicts to declare

Acknowledgments

This study was financially supported by KAKENHI (Grant Nos. No. 17H01341, 20H02518, and 20H02775) from the Japan Society for the Promotion of Science (JSPS) and by the Japanese Ministry of Education, Culture, Sports, Science, and Technology (MEXT) within the projects “Integrated Research Consortium on Chemical Sciences (IRCCS)” and “Elements Strategy Initiative to Form Core Research Center” (JPMXP0112101003). This study was also supported by the JST-CREST project JPMJCR17J3 and the Cooperative Research Program of Institute for Catalysis, Hokkaido University (19A1001 and 20B1004). S.Y. acknowledges Grant-in-Aid for JSPS Fellows (21J11744, DC2). The authors sincerely thank the technical division of the Institute for Catalysis (Hokkaido University) for manufacturing experimental equipment as well as the technical staff at the Open Facility of Hokkaido University for their assistance. Part of the calculations were conducted on supercomputers at RIIT (Kyushu Univ.).

REFERENCES

1 C. Copéret, A. Comas-Vives, M. P. Conley, D. P. Estes, A. Fedorov, V. Mougel, H. Nagae, F. Núnez-Zarur and P. A. Zhizhko, *Chem. Rev.*, 2016, **116**, 323–421.

2 C. Copéret, M. Chabanas, R. Petroff Saint-Arroman and J. M. Basset, *Angew. Chemie - Int. Ed.*, 2003, **42**, 156–181.

3 F. Müller, J. B. Stückrath, F. A. Bischoff, L. Gagliardi, J. Sauer, S. Debnath, M. Jorewitz and K. R. Asmis, *J. Am. Chem. Soc.*, 2020, **142**, 18050–18059.

4 D. Ray, S. Goswami, J. Duan, J. T. Hupp, C. J. Cramer and L. Gagliardi, *Chem. Mater.*, 2021, **33**, 1182–1189.

5 J. G. Vitillo, C. C. Lu, C. J. Cramer, A. Bhan and L. Gagliardi, *ACS Catal.*, 2021, **11**, 579–589.

6 X. Wang, X. Zhang, R. Pandharkar, J. Lyu, D. Ray, Y. Yang, S. Kato, J. Liu, M. C. Wasson, T. Islamoglu, Z. Li, J. T. Hupp, C. J. Cramer, L. Gagliardi and O. K. Farha, *ACS Catal.*, 2020, **10**, 8995–9005.

7 L. Liu and A. Corma, *Trends Chem.*, 2020, **2**, 383–400.

8 L. Liu and A. Corma, *Chem. Rev.*, 2018, **118**, 4981–5079.

9 S. Mitchell and J. Pérez-ramírez, *Nat. Commun.*, 2020, 10–12.

10 A. S. Hoffman, L. M. Debefve, S. Zhang, J. E. Perez-Aguilar, E. T. Conley, K. R. Justl, I. Arslan, D. A. Dixon and B. C. Gates, *ACS Catal.*, 2018, **8**, 3489–3498.

11 Y. Gu and W. S. Epling, *Appl. Catal. A Gen.*, 2019, **570**, 1–14.

12 J. Lee, J. R. Theis and E. A. Kyriakidou, *Appl. Catal. B Environ.*, 2019, **243**, 397–414.

13 M. Ozekmekci, G. Salkic and M. F. Fellah, *Fuel Process. Technol.*, 2015, **139**, 49–60.

14 M. Delkash, B. Ebrazi Bakhshayesh and H. Kazemian, *Microporous Mesoporous Mater.*, 2015, **214**, 224–241.

15 S. Wang and Y. Peng, *Chem. Eng. J.*, 2010, **156**, 11–24.

16 S. Brandenberger, O. Kröcher, A. Tissler and R. Althoff, *Catal. Rev.*, 2008, **50**, 492–531.

17 R. Zhang, N. Liu, Z. Lei and B. Chen, *Chem. Rev.*, 2016, **116**, 3658–3721.

18 P. Vanelderen, J. Vancauwenbergh, B. F. Sels and R. A. Schoonheydt, *Coord. Chem. Rev.*, 2013, **257**, 483–494.

19 A. M. Beale, F. Gao, I. Lezcano-Gonzalez, C. H. F. Peden and J. Szanyi, *Chem. Soc. Rev.*, 2015, **44**, 7371–7405.

20 E. Borfecchia, P. Beato, S. Svelle, U. Olsbye, C. Lamberti and S. Bordiga, *Chem. Soc. Rev.*, 2018, **47**, 8097–8133.

21 H. Saito and Y. Sekine, *RSC Adv.*, 2020, **10**, 21427–21453.

22 Z. Maeno, S. Yasumura, X. Wu, M. Huang, C. Liu, T. Toyao and K. Shimizu, *J. Am. Chem. Soc.*, 2020, **142**, 4820–4832.

23 G. Caeiro, R. H. Carvalho, X. Wang, M. A. N. D. A. Lemos, F. Lemos, M. Guisnet and F. Ramôa Ribeiro, *J. Mol. Catal. A Chem.*, 2006, **255**, 131–158.

24 N. Kosinov, C. Liu, E. J. M. Hensen and E. A. Pidko, *Chem. Mater.*, 2018, **30**, 3177–3198.

25 B. E. R. Snyder, P. Vanelderen, M. L. Bols, S. D. Hallaert, L. H. Böttger, L. Ungur, K. Pierloot, R. A. Schoonheydt, B. F. Sels and E. I. Solomon, *Nature*, 2016, **536**, 317–321.

26 U. Deka, I. Lezcano-Gonzalez, B. M. Weckhuysen and A. M. Beale, *ACS Catal.*, 2013, **3**, 413–427.

27 E. Borfecchia, K. A. Lomachenko, F. Giordanino, H. Falsig, P. Beato, A. V. Soldatov, S. Bordiga and C. Lamberti, *Chem. Sci.*, 2015, **6**, 548–563.

28 H. Li, C. Paolucci, I. Khurana, L. N. N. Wilcox, F. Göltl, J. D. Albarracin-Caballero, A. J. Shih, F. H. Ribeiro, R. Gounder and W. F. Schneider, *Chem. Sci.*, 2019, **10**, 2373–2384.

29 C. Liu, G. Li, E. J. M. Hensen and E. A. Pidko, *J. Catal.*, 2016, **344**, 570–577.

30 S. Li, Y. Wang, T. Wu and W. F. Schneider, *ACS Catal.*, 2018, **8**, 10119–10130.

31 A. Boubnov, H. W. P. Carvalho, D. E. Doronkin, T. Gu, E. Gallo, A. J. Atkins, C. R. Jacob and J. Grunwaldt, *J. Am. Chem. Soc.*, 2014, **136**, 13006–13015.

32 C. Paolucci, A. A. Parekh, I. Khurana, J. R. Di Iorio, H. Li, J. D. Albarracin Caballero, A. J. Shih, T. Anggara, W. N. Delgass, J. T. Miller, F. H. Ribeiro, R. Gounder and W. F. Schneider, *J. Am. Chem. Soc.*, 2016, **138**, 6028–6048.

33 D. K. Pappas, E. Borfecchia, M. Dyballa, I. A. Pankin, K. A. Lomachenko, A. Martini, M. Signorile, S. Teketel, B. Arstad, G. Berlier, C. Lamberti, S. Bordiga, U. Olsbye, K. P. Lillerud, S. Svelle and P. Beato, *J. Am. Chem. Soc.*, 2017, **139**, 14961–14975.

34 K. T. Dinh, M. M. Sullivan, K. Narsimhan, P. Serna, R. J. Meyer, M. Dincă and Y. Román-Leshkov, *J. Am. Chem. Soc.*, 2019, **141**, 11641–11650.

35 N. A. Grosso-Giordano, A. S. Hoffman, A. Boubnov, D. W. Small, S. R. Bare, S. I. Zones and A. Katz, *J. Am. Chem. Soc.*, 2019, **141**, 7090–7106.

36 M. L. Bols, S. D. Hallaert, B. E. R. Snyder, J. Devos, D. Plessers, H. M. Rhoda, M. Dusselier, R. A. Schoonheydt, K. Pierloot, E. I. Solomon and B. F. Sels, *J. Am. Chem. Soc.*, 2018, **140**, 12021–12032.

37 M. Ogura, S. Kage, T. Shimojo, J. Oba, M. Hayashi, M. Matsukata and E. Kikuchi, *J. Catal.*, 2002, **211**, 75–84.

38 K. Shimizu, F. Okada, Y. Nakamura, A. Satsuma and T. Hattori, *J. Catal.*, 2000, **195**, 151–160.

39 A. Ali, W. Alvarez, C. J. Loughran and D. E. Resasco, *Appl. Catal. B Environ.*, 1997, **14**, 13–22.

40 R. Villamaina, U. Iacobone, I. Nova, E. Tronconi, M. P. Ruggeri, L. Mantarosie, J. Collier and D. Thompsett, *Appl. Catal. B Environ.*, 2021, **284**, 119724.

41 H.-Y. Chen, S. Mulla, E. Weigert, K. Camm, T. Ballinger, J. Cox and P. Blakeman, *SAE Int. J. Fuels Lubr.*, 2013, **6**, 372–381.

42 Coulson, J.E., Brisley, R.J., Keane, O., Phillips, P.R., and Mountstevens, E.H., Patent application,WO 2008/047170, 2008, .

43 K. Khivantsev, N. R. Jaegers, L. Kovarik, S. Prodinger, M. A. Derewinski, Y. Wang, F. Gao and J. Szanyi, *Appl. Catal. A Gen.*, 2019, **569**, 141–148.

44 K. Khivantsev, N. R. Jaegers, I. Z. Koleva, H. A. Aleksandrov, L. Kovarik, M. Engelhard, F. Gao, Y. Wang, G. N. Vayssilov and J. Szanyi, *J. Phys. Chem. C*, 2020, **124**, 309–321.

45 Y. Zheng, L. Kovarik, M. H. Engelhard, Y. Wang, Y. Wang, F. Gao and J. Szanyi, *J. Phys. Chem. C*, 2017, **121**, 15793–15803.

46 H.-Y. Chen, J. E. Collier, D. Liu, L. Mantarosie, D. Durán-Martín, V. Novák, R. R. Rajaram and D. Thompsett, *Catal. Letters*, 2016, **146**, 1706–1711.

47 J. Lee, Y. Ryou, S. Hwang, Y. Kim, S. J. Cho, H. Lee, C. H. Kim and D. H. Kim, *Catal. Sci. Technol.*, 2019, **9**, 163–173.

48 Y. Gu, S. Marino, M. Cortés-Reyes, I. S. Pieta, J. A. Pihl and W. S. Epling, *Ind. Eng. Chem. Res.*, , DOI:10.1021/acs.iecr.0c05186.

49 K. Mandal, Y. Gu, K. S. Westendorff, S. Li, J. A. Pihl, L. C. Grabow, W. S. Epling and C. Paolucci, *ACS Catal.*, 2020, **10**, 12801–12818.

50 J. Lee, Y. S. Ryou, S. J. Cho, H. Lee, C. H. Kim and D. H. Kim, *Appl. Catal. B Environ.*, 2018, **226**, 71–82.

51 K. Khivantsev, N. R. Jaegers, L. Kovarik, J. C. Hanson, F. (Feng) Tao, Y. Tang, X. Zhang, I. Z. Koleva, H. A. Aleksandrov, G. N. Vayssilov, Y. Wang, F. Gao and J. Szanyi, *Angew. Chemie - Int. Ed.*, 2018, **57**, 16672–16677.

52 Y. S. Ryou, J. Lee, S. J. Cho, H. Lee, C. H. Kim and D. H. Kim, *Appl. Catal. B Environ.*, 2017, **212**, 140–149.

53 K. Khivantsev, M. A. Derewinski, N. R. Jaegers, D. Boglaienko, P. Hernandez, C. Pearce, Y. Wang and J. Szanyi, *ChemRxiv*, 2021, **Preprint,** DOI: 10.26434/chemrxiv.14038388.v1.

54 T. M. Lardinois, J. S. Bates, H. H. Lippie, C. K. Russell, J. T. Miller, H. M. Meyer, K. A. Unocic, V. Prikhodko, X. Wei, C. K. Lambert, A. B. Getsoian and R. Gounder, *Chem. Mater.*, 2021, acs.chemmater.0c04465.

55 K. Khivantsev, N. R. Jaegers, L. Kovarik, J. C. Hanson, F. (Feng) Tao, Y. Tang, X. Zhang, I. Z. Koleva, H. A. Aleksandrov, G. N. Vayssilov, Y. Wang, F. Gao and J. Szanyi, *Angew. Chemie Int. Ed.*, 2018, **57**, 16672–16677.

56 S. Yasumura, H. Ide, T. Ueda, Y. Jing, C. Liu, K. Kon, T. Toyao, Z. Maeno and K. Shimizu, *JACS Au*, 2021, **1**, 201–211.

57 G. Kresse and J. Hafner, *Phys. Rev. B*, 1993, **48**, 13115–13118.

58 G. Kresse and J. Hafner, *Phys. Rev. B*, 1994, **49**, 14251–14269.

59 G. Kresse and J. Furthmüller, *Phys. Rev. B*, 1996, **54**, 11169–11186.

60 P. E. Blöchl, *Phys. Rev. B*, 1994, **50**, 17953–17979.

61 D. Kresse, G.; Joubert, G. Kresse and D. Joubert, *Phys. Rev. B*, 1999, **59**, 1758–1775.

62 H. J. Monkhorst and J. D. Pack, *Phys. Rev. B*, 1976, **13**, 5188–5192.

63 C. Baerlocher and L. B. McCusker, Database of Zeolite Structures, http://www.iza-structure.org/databases, (accessed 10 June 2019).

64 J. Da Chai and M. Head-Gordon, *Phys. Chem. Chem. Phys.*, 2008, **10**, 6615–6620.

65 N. Mardirossian and M. Head-Gordon, *Mol. Phys.*, 2017, **115**, 2315–2372.

66 E. Mansoor, M. Head-Gordon and A. T. Bell, *ACS Catal.*, 2018, **8**, 6146–6162.

67 F. Weigend and R. Ahlrichs, *Phys. Chem. Chem. Phys.*, 2005, **7**, 3297–3305.

68 F. Weigend, *Phys. Chem. Chem. Phys.*, 2006, **8**, 1057–1065.

69 T. Lu and F. Chen, *J. Comput. Chem.*, 2012, **33**, 580–592.

70 J. R. Di Iorio and R. Gounder, *Chem. Mater.*, 2016, **28**, 2236–2247.

71 J. R. Di Iorio, S. Li, C. B. Jones, C. T. Nimlos, Y. Wang, E. Kunkes, V. Vattipalli, S. Prasad, A. Moini, W. F. Schneider and R. Gounder, *J. Am. Chem. Soc.*, 2020, **142**, 4807–4819.

72 J. R. Di Iorio, C. T. Nimlos and R. Gounder, *ACS Catal.*, 2017, **7**, 6663–6674.

73 M. Dusselier and M. E. Davis, *Chem. Rev.*, 2018, **118**, 5265–5329.

74 K. Mlekodaj, J. Dedecek, V. Pashkova, E. Tabor, P. Klein, M. Urbanova, R. Karcz, P. Sazama, S. R. Whittleton, H. M. Thomas, A. V. Fishchuk and S. Sklenak, *J. Phys. Chem. C*, 2019, **123**, 7968–7987.

75 J. Dědeček, E. Tabor and S. Sklenak, *ChemSusChem*, 2019, **12**, 556–576.

76 S. Li, H. Li, R. Gounder, A. Debellis, I. B. Müller, S. Prasad, A. Moini and W. F. Schneider, *J. Phys. Chem. C*, 2018, **122**, 23564–23573.

77 J. Van der Mynsbrugge, M. Head-Gordon and A. T. Bell, *J. Mater. Chem. A*, 2021, **9**, 2161–2174.

78 R. Grybos, J. Hafner, L. Benco and P. Raybaud, *J. Phys. Chem. C*, 2008, **112**, 12349–12362.

79 T. Kamachi, T. Tatsumi, T. Toyao, Y. Hinuma, Z. Maeno, S. Takakusagi, S. Furukawa, I. Takigawa and K. Shimizu, *J. Phys. Chem. C*, 2019, **123**, 20988–20997.

80 S. Dapprich and G. Frenking, *J. Phys. Chem. C*, 1995, **99**, 9352–9362.

81 B. Kalita and R. C. Deka, *Catal. Letters*, 2010, **140**, 205–211.

82 C. Descorme, P. Gélin, C. Lécuyer and M. Primet, *J. Catal.*, 1998, **177**, 352–362.

83 K. K. Irikura, *J. Phys. Chem. Ref. Data*, 2007, **36**, 389–397.

84 C. Amiot, *J. Mol. Spectrosc.*, 1982, **94**, 150–172.

85 E. Bello, V. J. Margarit, E. M. Gallego, F. Schuetze, C. Hengst, A. Corma and M. Moliner, *Microporous Mesoporous Mater.*, 2020, **302**, 110222.

86 S. Yasumura, C. Liu, T. Toyao, Z. Maeno and K. Shimizu, *J. Phys. Chem. C*, 2021, **125**, 1913–1922.

87 P. A. Redhead, *Vacuum*, 1962, **12**, 274.